

MMEarth: Exploring Multi-Modal Pretext Tasks For Geospatial Representation Learning

Vishal Nedungadi¹, Ankit Kariryaa¹, Stefan Oehmcke¹, Serge Belongie²,
Christian Igel¹, and Nico Lang¹

University of Copenhagen, Denmark
vishalned@gmail.com, nila@di.ku.dk

Abstract. The volume of unlabelled Earth observation (EO) data is huge, but many important applications lack labelled training data. However, EO data offers the unique opportunity to pair data from different modalities and sensors automatically based on geographic location and time, at virtually no human labor cost. We seize this opportunity to create a diverse multi-modal pretraining dataset at global scale. Using this new corpus of 1.2 million locations, we propose a *Multi-Pretext Masked Autoencoder (MP-MAE)* approach to learn general-purpose representations for optical satellite images. Our approach builds on the ConvNeXt V2 architecture, a fully convolutional masked autoencoder (MAE). Drawing upon a suite of multi-modal pretext tasks, we demonstrate that our MP-MAE approach outperforms both MAEs pretrained on ImageNet and MAEs pretrained on domain-specific satellite images. This is shown on several downstream tasks including image classification and semantic segmentation. We find that multi-modal pretraining notably improves the linear probing performance, *e.g.* 4pp on BigEarthNet and 16pp on So2Sat, compared to pretraining on optical satellite images only. We show that this also leads to better label and parameter efficiency which are crucial aspects in global scale applications. ¹

Keywords: representation learning, self-supervised learning, multi-modal, multi-task, masked autoencoder, Earth observation, remote sensing, satellite images, Sentinel-2

1 Introduction

Learning representations through self-supervision has seen major advancements in recent years [2, 5, 22, 32, 33]. This gives hope that even applications with limited supervision data may profit from the promises of the deep learning revolution. However, some self-supervised techniques still fall short when evaluated on image domains other than ImageNet, *e.g.*, ground-level images from the natural

¹ The MMEarth dataset is available on the project page: vishalned.github.io/mmeearth. The dataset construction code is available here: github.com/vishalned/MMEarth-data. The MP-MAE code for training and evaluation is available here: github.com/vishalned/MMEarth-train.

world [47]. Thus, to develop generalizing representation learning techniques, it is necessary to have suitable large-scale datasets of different domains. As an alternative to “pure” self-supervision paradigm, multi-modal data offer great potential for learning good semantic representations [4,31,36]. Aligned multi-modal datasets are key for advancing two major research directions in computer vision: i) exploiting multi-modal data for representation learning, and ii) advancing representation learning to exploit multi-modal data for inference.

One domain that is particularly well-suited for studying the potential of multi-modal data is Earth Observation (EO). Geolocated data from different sensors can automatically be aligned at virtually no human labor cost. Aligning such EO data at large scale became substantially easier thanks to cloud-based platforms like Google Earth Engine [21] and Microsoft Planetary Computer [30]. Furthermore, real-world remote sensing applications are often hampered by a lack of high-quality reference data. Human annotation of satellite data is not always possible from the images alone, for example when mapping carbon stocks or species abundance. Such applications require field measurements by experts that are costly, time consuming, and do not scale to large areas. Other high-quality measurement systems, such as airborne or spaceborne LiDAR, can provide a means to scale reference data, but still provide a biased sample of the Earth, due to the limits of global sampling. Here, we present a global dataset called *MMEarth* at the scale of ImageNet-1k [13] with multi-modal data for 1.2M locations. We also release our data collection framework that allows to collect data from different sensors given a list of geospatial coordinates. While *MMEarth* can be used to advance both aforementioned research directions, we demonstrate its potential for the first goal of exploiting multi-modal data for improving representation learning. Specifically, our goal is to learn general-purpose representations for optical satellite images from the Sentinel-2 mission that are predictive for a wide range of downstream tasks including crop type, landcover, and climate zone classification. Thus, in contrast to other work in this area, we neither aim to generalize to other sensor inputs such as Scale-MAE [37] nor to make use of multiple modalities at inference during downstream tasks as MultiMAE [4] or 4M [31]. As shown by previous work, specializing a model to a particular input modality can be beneficial compared to models that aim to generalize to multiple input modalities [31].

To explore the potential of multiple pretext tasks, we build on fully convolutional masked autoencoders (FCMAE) and extend the ConvNeXt V2-MAE approach [52] with multi-modal reconstruction tasks for pretraining. As opposed to MAEs based on vision transformers, the FCMAE is well suited for downstream tasks that require different input image sizes, which is a inevitable when evaluating the representations on existing EO benchmarks [27]. Intuitively, such a multi-task pretraining strategy with a shared encoder should lead to representations that generalize better to new downstream tasks that are not known at pretraining time. We evaluate the potential for new downstream tasks on the GEO-Bench [27] Sentinel-2 tasks including image-level multi-class as well as

multi-label classification and semantic segmentation. Our contributions can be summarized as follows:

1. **MMEarth dataset** - A global dataset for multi-modal and geospatial representation learning. It consists of 12 modalities including pixel-level and image-level modalities from 1.2 million locations.
2. **Method** - We explore the effect of multi-modal pretext tasks for both pixel-level and image-level modalities when learning general purpose representations for interpreting optical images from Sentinel-2. Therefore, we propose a Multi-Pretext Masked Autoencoder (MP-MAE) approach to use MMEarth to learn better representations for Sentinel-2 optical images.
3. **Results** - We show that pretraining MP-MAE on MMEarth outperforms not only MAEs pretrained on ImageNet but also on Sentinel-2 images. While both fine-tuning and linear probing performance is improved, linear probing profits substantially from the multi-modal pretext tasks.

2 Related work

2.1 Masked image modelling

Masked Image Modelling (MIM) can see its roots in denoising autoencoders that are trained to reconstruct original images from partially corrupted inputs [49]. This idea was extended to pretrain CNN autoencoders by reconstructing a large area in an image with the aim to learn better representations by conditioning a portion of the image on its surroundings [34]. With the success of masked language modelling (for example, BERT [14]) and the rise of Vision Transformers (ViT) [16], Masked Autoencoder (MAE) approaches have been developed that reconstruct masked input patches [16, 22, 53]. When masking a large fraction of the input sequence, MIM is not only a successful pretext task to learn semantic representations, but also leads to a more efficient ViT encoder [22, 53]. This masking strategy has also been extended to spatio-temporal modelling to learn from videos [6, 18, 44, 51] as well as to learn representations for 3D point clouds [55]. To combine this random masking strategy with the inductive bias of CNNs, we use ConvNeXt V2 [52] which is a Fully Convolutional MAE (FCMAE). The encoder is implemented with sparse convolutions [9] to improve efficiency like in the ViT-based MAE. ConvNeXt V2 also uses a learnable mask token which serves as the input to the convolutional decoder. Instead of using self-attention, the decoder is based on dense convolutions with kernels that cover the full spatial extent of the image. This architecture design pretrained on ImageNet, leads to a high-performing model family of different sizes, ranging from 3.7M (‘Atto’) to 650M parameters (‘Huge’). We adapt the ConvNeXt V2 architecture design to satellite images and pretrain on our MMEarth dataset to demonstrated the potential of multi-modal EO data for representation learning.

2.2 Multi-modal representation learning

Multi sensory information has been argued to help humans (and animals) to understand the natural world [40], which motivates the development of machine

learning approaches that learn representations from multi-modal data. Successful approaches such as CLIP [36] are based on a contrastive learning objective while learning separate encoders for each input modality. This approach has been extended to learn from images, text, and audio extracted from videos [1]. While contrastive approaches usually rely on aligned samples from various modalities, non-contrastive approaches were proposed to *e.g.* learn image-text representations with a single encoder to avoid the need for paired image-text data [19]. It has been shown that visual tasks are (more or less) related and that it can be more data efficient to learn multiple tasks jointly [56]. In line with these observations, multi-task self-training [20] leverages pseudo-labels for multi-task learning to yield improved general purpose representations. In addition to such multi-task objectives, MIM has been extended to the multi-modal image setting [4, 31, 51]. Masked feature prediction [51] has been demonstrated as an effective pretext task, *e.g.* by reconstructing the Histograms of Oriented Gradients (HOG) instead of the original image, arguing that the local contrast normalization plays a crucial role. MultiMAE [4] extends the MAE approach [22] to multiple input and output modalities using RGB, semantic label masks, and depth. Recently, 4M [31] proposed a masked modelling framework to train a single autoencoder for a range of input and output modalities. Instead of reconstructing each modality in the original space (*e.g.* pixels for RGB), each modality is first mapped to discrete tokens using a modality-specific autoencoder. These tokens are then used as the input and output to a transformer-based autoencoder trained with masked modelling leading to impressive any-to-any reconstruction results. However, their ablation study demonstrates that pretraining with a single input modality can outperform a model trained with multiple input modalities. While previous works have focused on image modalities that provide pixel-level data, our approach makes use of both pixel-level and image-level modalities.

2.3 Representation learning in Earth observation

Supervised learning at large scale. In applications where labelled training data is abundant, supervised learning has been used in a range of applications like tree segmentation [46], marine debris detection [39], or snow depth estimation [12]. However, only few studies have scaled supervised deep learning to global scales to map land cover [8], canopy height [28], or solar panels [26]. Additionally, large annotated EO datasets have been created to replace ImageNet with a domain-specific pretraining dataset [7, 10, 41, 42, 50]. Some bi-modal datasets provide Sentinel-2 optical and Sentinel-1 SAR images in Europe [42] and globally around cities [50]. In contrast, MMEarth provides a global pretraining dataset with 12 modalities balanced across 14 biomes [15].

Self-supervised learning. Self-supervised approaches developed on ground-level computer vision benchmarks (like ImageNet) can be applied to satellite images [43, 50]. However, these approaches might be suboptimal due to the differences in ground-level and satellite images. Therefore, the EO community has

started to explore the unique opportunities offered by EO data. We consider three major aspects of EO data for self-supervised representation learning: *geolocation*, *time*, and *modality*.

Geolocation. In an approach called geography-aware self-supervised learning (GASSL) [3], the contrastive learning objective leverages the spatio-temporal structure of EO data. Using spatially aligned images, positive image pairs can be created by using observations at different times, avoiding the need of artificial augmentations. In addition, localization is used as a pretext task by predicting the clusters of sampled locations. SatCLIP [25] focuses on learning location embeddings in a contrastive manner by learning a Sentinel-2 encoder and a location encoder with a contrastive objective. **Time.** Seasonal contrast (SeCo [29]) is another temporal contrastive approach that learns multiple embedding subspaces that are invariant to either seasonal changes, synthetic augmentations, or all transformations. Alternatively, image time series can be exploited in masked modelling like demonstrated in SatMAE [11]. Presto [45] is a masked modelling approach that focuses on learning representations for multi-modal time series using a light-weight transformer architecture, which only relies on pixel time series inputs, but ignores textural features. **Modality.** Scale-MAE [37] aims to generalize to different input resolutions by conditioning on the ground sampling distance (GSD, size of a pixel on the ground). Most related to our work is SatlasPretrain [7], a large multi-task dataset for optical satellite images including Sentinel-2. Their goal was “*to label everything that is visible in a satellite image*” using various data sources (Open Street Map, lidar scans, landcover maps) and human annotators (domain experts and Mechanical Turk workers). Our MMEarth dataset creation differs, as it is fully automatic without relying on human annotators and also considers modalities that are not *explicitly visible for humans* in the optical images. Such modalities include everything that cannot be annotated by a human like radar, temperature, precipitation, or canopy height. We hypothesize that predicting such cross-modal relations from images requires the extraction of semantic features.

All these works provide important insights in how to make better use of satellite data and its metadata in representation learning. Our work extends along the last aspect — exploiting multiple modalities — whereas space and time serve as the underlying structure to pair data from different sources automatically without relying on human annotation. Furthermore, we treat geolocation and time as two additional modalities in our framework.

3 MMEarth dataset

MMEarth contains data for 1.2 million locations distributed around the world, making its optical image count comparable to ImageNet-1K [13]. At each location, data from 12 geo-aligned modalities were collected, grouped into pixel-level and image-level modalities, see Table 1. The six pixel-level modalities represent raster data of size 128×128 pixels which capture $1.28 \text{ km} \times 1.28 \text{ km}$ on the ground (*e.g.*, Sentinel-2, Sentinel-1, Aster DEM, Dynamic World, and ESA

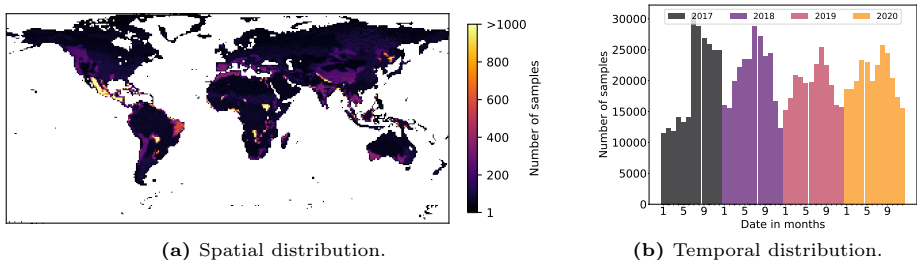


Fig. 1: MMEarth dataset coverage. With a balanced sampling scheme across 14 biomes and 4 years, we collected aligned multi-modal data from 12 modalities using the Google Earth Engine platform [21] at 1.2M locations.

Table 1: Modalities in the MMEarth dataset. Each location provides 12 aligned modalities with a total of 46 bands. The upper half of the modalities provides dense data at the pixel-level and the bottom half at the image-level.

	Sensor/Product	Description	Data type	#Bands	Band information
Pixel-level	Sentinel-2	Optical	continuous	12	multi-spectral B1-B12 for L1C/L2A product
	Sentinel-1	SAR	continuous	8	VV, VH, HV, HH for ascending/descending orbit
	Aster DEM	Elevation	continuous	2	elevation, slope
	ETH-GCHM	Vegetation height	continuous	2	canopy height, uncertainty (STD)
	Dynamic World	Landcover	categorical	1	9 landcover categories
	ESA World Cover	Landcover	categorical	1	11 landcover categories
Image-level	Biome	Landcover	categorical	1	14 terrestrial ecosystem categories
	Ecoregion	Landcover	categorical	1	846 ecoregion categories
	ERA5 temperature	Climate reanalysis	continuous	9	mean, min, and max of [year, month, previous month]
	ERA5 precipitation	Climate reanalysis	continuous	3	total precipitation of [year, month, previous month]
	Geolocation	Latitude, Longitude	continuous	4	cyclic encoding of latitude and longitude
	Date (Sentinel-2)	Month of the year	continuous	2	cyclic encoding of the month

World Cover). The remaining six image-level modalities represent scalar values for each location (*e.g.*, Biome, Ecoregion, ERA5 temperature, ERA5 precipitation, Geolocation, and Sentinel-2 observation date). The size of the input images is large enough for typical downstream EO tasks [27] and yields a reasonable dataset volume. MMEarth was sampled uniformly across 14 biomes (Fig. 1, *e.g.*, Mangroves, Temperate Conifer Forests, Tundra, etc.) [15]. To increase diversity, we considered data from the four years 2017–2020 (Fig. 1). Further, we ensured that time-critical modalities were collected around the Sentinel-2 observation date, which serves as the reference. Additionally, all pixel-level modalities were re-projected to the Sentinel-2 10m grid, if needed, yielding a harmonized data cube. In addition to the full dataset, we provide two ‘taster’ subsets to facilitate research in multi-modal representation learning with limited compute resources: *MMEarth100k* (100k locations at 128×128 pixels) and *MMEarth64* (1.2M locations center cropped to 64×64 pixels), see supplementary material for details. All the data were downloaded from Google Earth Engine (GEE) [21]. In the following subsections, we provide a brief overview of the pixel-level and image-level modalities listed in Table 1. More details in the supplementary material.

3.1 Pixel-level modalities

Sentinel-2. An optical satellite mission that provides global coverage at least every 5 days at 10m resolution. Its multi-spectral sensor comprises of 12 bands, with four bands RGBN (RGB and near infrared) at 10m and near and short-wave infrared bands at 20m and 60m resolution, respectively. We upsample all bands to the 10m grid. Sentinel-2 provides two processing levels: top of atmosphere reflectance (L1C) and the bottom of atmosphere reflectance (L2A). L2A is atmospherically corrected, harmonizing the spectral data, but is not yet available for all years on a global scale. To ensure global coverage for the years 2017–2020, MMEarth includes both L2A and L1C data. **Sentinel-1.** Synthetic Aperture Radar (SAR) data at 10m resolution, collected in two viewing directions along an ascending and descending orbit, resulting in four bands each. **Aster GDEM.** A Global Digital Elevation Model derived from the Advanced Spaceborne Thermal Emission and Reflection Radiometer (ASTER). The Aster GDEM data covers 99% of the Earth’s landmass at 15m resolution. We include elevation and slope. **ETH-GCHM.** A 10m Global Canopy Top Height Map [28] for the year 2020 derived from Sentinel-2 and sparse vertical structure data from GEDI [17], a spaceborne lidar mission. **Dynamic World.** A land cover dataset that contains semantic segmentation of Sentinel-2 images for nine categories at 10m resolution. We aggregate the per image maps for each year to reduce noise in the data. **ESA World Cover.** A 10m global land cover map based on Sentinel-1 and Sentinel-2 data with 11 categories for the year 2020.

3.2 Image-level modalities

Biome. A Biome is a geographical region with specific vegetation, climate and animal life. We use the RESOLVE Ecoregions dataset [15] that consists of 14 terrestrial biomes. **Ecoregion.** The RESOLVE ecoregions [15] include 846 terrestrial ecoregions. These are a more fine-grained classification than biomes. For example the ecoregions *Central African Mangroves* and *Indochina Mangroves* belong to the biome *Mangroves*. **ERA5 Temperature and Precipitation.** ERA5 reanalysis data provides climate information back to 1950. Based on the Sentinel-2 observation date, we collect the corresponding mean, min, and max temperature as well as the total precipitation for the month, previous month, and year. **Geolocation.** We use cyclic encodings for the latitude and longitude of each image center. This ensures that for the longitude the cyclic property is maintained (transition from West to East). **Date.** We use a cyclic encoding of the month of the Sentinel-2 observation date as a proxy for the season.

4 Methodology

4.1 Multi-Pretext Masked Autoencoder

In this section, we describe the proposed Multi-Pretext Masked Autoencoder (MP-MAE) approach as illustrated in Fig. 2. It builds on the promising results of MIM with the ConvNeXt V2 architecture.

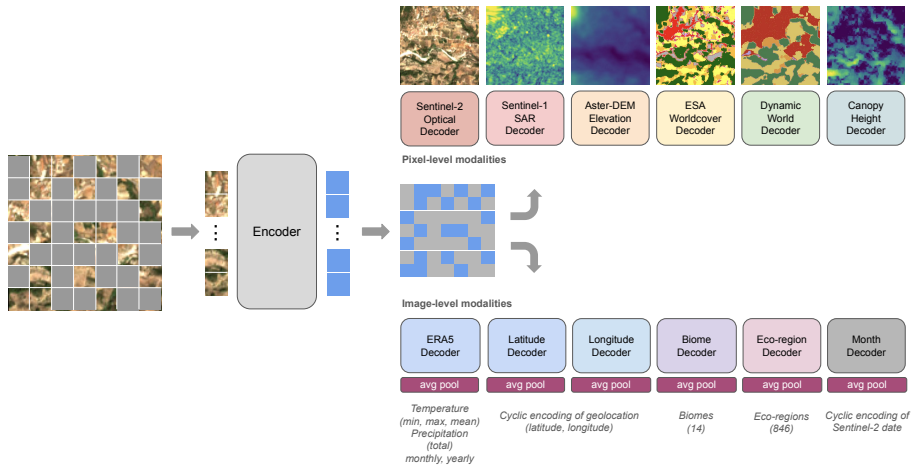


Fig. 2: Multi-Pretext Masked Autoencoder (MP-MAE). Our approach extends Masked Autoencoders, which reconstruct only the input image, by incorporating multiple pretext tasks using aligned pixel-level as well as image-level modalities.

Encoder. The input image x is divided into patches (or tokens) on which a random mask is applied to yield a masked image x' . The encoder f_θ takes the visible patches as the input and returns an encoding z for every visible patch. Here, the ConvNeXt V2 [52] architecture serves as the backbone which is implemented with sparse convolutions [9] to improve efficiency. We investigate two key modifications to adapt the ConvNeXt V2 architecture to medium-resolution satellite images. First, we adapted the patch size. The original ConvNeXt V2-MAE has been developed for pretraining on ImageNet and assumes input images of size 224×224 pixels, which are split into 7×7 patches of size 32×32 pixels. MMEarth images are of size 128×128 pixels, and we randomly crop them to 112×112 pixels when feeding them into the MP-MAE encoder, which has a reduced patch size of 16×16 pixels to preserve the 7×7 patch layout. This adjustment is crucial as the number of patches is coupled with the optimal masking ratio. Second, we avoid early downsampling by modifying the first layer. In the original ConvNeXt V2 encoder, the first layer is a learned convolutional downsampling, which yields feature maps at $1/4$ of the input resolution. While this approach might be efficient and loses only little spatial information that is not needed for ImageNet classification, it may not be optimal for medium-resolution satellite images such as Sentinel-2 and for pixel-level downstream tasks such as semantic segmentation with U-Net architectures [38], where high-resolution features can inform same-resolution representations via the skip connections. Therefore, we replace the first layer with an initial convolutional layer with kernel size 3 and stride 1 to learn feature maps at the input resolution followed by a depth-wise convolutional downsampling layer.

Decoders. We follow the ConvNeXt V2-MAE [52] decoder design and use shallow decoders with one block. We apply the same random mask to all pixel-level modalities and learn a separate decoder h_t for each task. We consider T tasks and treat most modalities as individual tasks, but group the climate variables and split latitude and longitude (see Fig. 2). To reconstruct the masked patches, a learnable mask token is used as a placeholder when combining the embedding tokens to get a dense 2D-input for the decoders. Therefore, the decoders are based on standard convolutions. For the image-level modalities, we introduce a global average pooling over the decoded non-visible patches before the final linear prediction layer. Hence, we follow the same strategy as for pixel-level modalities, whereas the encoder is encouraged to learn representations that provide the semantic context that is needed to decode the masked tokens.

4.2 Multi-task loss

All task targets y_t are reconstructed by applying the same random mask to avoid that the model learns any shortcuts between the input and the targets. We follow prior work and compute the losses only over non-visible patches. We experimented with two settings for the multi-task loss function [24, 48]

$$\mathcal{L} = \sum_{t=1}^T \frac{1}{\hat{\sigma}_t^2} \mathcal{L}_t(h_t(f_\theta(x)), y_t) + \log \hat{\sigma}_t, \quad (1)$$

with task-specific loss \mathcal{L}_t (*e.g.*, cross entropy for classification and mean squared error for regression) and variance $\hat{\sigma}_t^2$. First, we applied equal weighting with $\hat{\sigma}_t^2 = 1$ for all decoders, followed by task-uncertainty weighting where $\hat{\sigma}_t^2$ is learnable for each decoder [4, 24]. The second setting was expected to aid in handling noisy targets, as task-specific weights naturally decrease for such tasks [24].

5 Experimental setup

Given a pretrained encoder, we followed standard practices and evaluated fine-tuning (FT) and linear probing (LP) performance on new downstream tasks. While both approaches learn the last linear layer of a neural network from scratch, FT updates the pretrained encoder and LP uses a frozen encoder.

5.1 Evaluation on downstream tasks

For downstream tasks, we considered all five Sentinel-2 datasets provided in the GEO-Bench [27] EO dataset collection. These datasets provide a diverse set of tasks and geographical coverage (Global, Europe, Africa). GEO-Bench provides harmonized subsets of the original datasets with comparable training set sizes and balanced class distributions. For clarity, we refer to the datasets with the number of training samples to avoid confusion with prior work using the original

Table 2: Downstream task datasets. We evaluated on five different datasets which involve image-level classification (multi-label, multi-class) and pixel-level semantic segmentation. These datasets are modified versions from the GeoBench benchmark [27].

Dataset Name	Description	Task	Categories	Input [px]	Train/Val/Test
BigEarth20k [41]	Landcover classification in Europe	Multi-label	43	120×120	20k/1k/1k
So2Sat20k [57]	Global local climate zones classification	Multi-class	17	32×32	20k/1k/1k
EuroSat16k [23]	Landcover classification in Europe	Multi-class	10	64×64	16k/1k/1k
Cashew1k [54]	Cashew plantations in Benin (Africa)	Segmentation	7	256×256	1.3k/400/50
SAcrop3k [35]	Crop-type segmentation in South Africa	Segmentation	10	256×256	3k/1k/1k

datasets. We summarize the characteristics of these five datasets in Table 2 and provide more details in the following sections.

Image classification: BigEarthNet [41] is a multi-label land cover classification problem with 43 categories and data from 10 countries in Europe. While the original dataset contains a total of 590k Sentinel-2 image samples, the GEO-Bench version, referred to as ‘BigEarth20k’, contains 20k training samples. **So2Sat** [57] is a multi-class land cover classification task with 17 categories that classifies local climate zones. The data is collected globally from urban areas and the original data contains 400k pairs of Sentinel-2 and Sentinel-1 image samples. The GEO-Bench version contains 20k training samples and is referred to as ‘So2Sat20k’. **EuroSat** [23] is a multi-class land use and land cover classification dataset covering Europe with 10 categories. The original dataset contains 27k image samples, and the GEO-Bench version ‘EuroSat16k’ has roughly 16k training samples. As evaluation metrics, we use the overall accuracy (Acc) for multi-class and the mean average precision (mAP) for multi-label classification. **Semantic segmentation: Cashew Plantation** [54] is semantic segmentation task with 7 categories that maps cashew plantations in Benin, Africa. The ‘Cashew1k’ consists of 1k training samples. **SA-Crop-Type** [35] is another semantic segmentation problem with 10 categories that maps crop type in South Africa. The ‘SAcrop3k’ consists of 3k training samples.

5.2 Implementation details

Pretraining: We mainly followed the ConvNeXt V2 hyperparameter settings. If not stated otherwise, we pretrained for 200 epochs with a base learning rate $1.5 \cdot 10^{-4}$ and an effective batch size of 4096. The only data augmentation used was random cropping. We standardize each channel in the input and targets to zero mean and unit variance on the pretraining data. To harmonize the two Sentinel-2 products, we standardize L1C and L2A individually. The target normalization harmonizes the losses for modalities with shared characteristics (*e.g.* continuous targets). Missing input pixels are replaced by zeros (*i.e.* the mean). Local target patch normalization is used for reconstructing the optical image bands [22].

Fine-tuning parameters: We fine-tuned and linear probed for 100 epochs, and maintained an effective batch size of 1024 with a base learning rate of $2 \cdot 10^{-4}$.

For the semantic segmentation tasks we fine-tuned (FT) in two phases. First, we trained the randomly initialized U-Net decoder with the frozen pretrained encoder for 50 epochs, and then fine-tuned the full model for another 150 epochs. We maintained an effective batch size of 32, and a base learning rate of 0.01. We did not apply any data augmentation.

Semantic segmentation We adopt a U-Net [38] architecture to evaluate the pretrained encoders. The upsampling block consists of a nearest neighbour upsampling followed by a convolutional layer with 3×3 filter kernels, layer norm and a GELU activation layer.

6 Results

We investigated two research questions: *How can domain specific pretraining improve representations?* and *How do multi-modal pretext tasks impact representations?*

6.1 How can domain specific pretraining improve representation?

Switching to domain specific data is not enough. Results from Table 3 indicate that just replacing the ImageNet pretraining data with domain specific optical satellite images does not improve downstream performance. We propose to slightly adjust the encoder design and the patch size to adapt to medium resolution satellite images like Sentinel-2 (10m pixels on the ground). Reducing the patch size from 32 to 16 pixels is crucial to adapt to the smaller image size of the medium resolution satellite images. This preserves the number of patches to be 7×7 as in the original ConvNeXt V2 ImageNet setting and is related to an optimal masking ratio [53]. With these modifications, domain specific pretraining improved fine-tuning performance across all datasets compared to pretraining on ImageNet. While linear probing (LP) on BigEarth20k was also improved by 5pp, pretraining on ImageNet provides a strong LP baseline for So2Sat20k.

Multi-spectral images are beneficial. Since Sentinel-2 images provide more than RGB bands, we studied the impact of pretraining on multi-spectral images and found that this can improve downstream performance depending on the tasks. Both segmentation tasks profited most from the multi-spectral pretraining each with 3.5pp improvement over the RGB pretraining. We hypothesize that this is not due to the fact that these are segmentation tasks, but rather that ambiguous crop types can profit from the additional spectral information.

6.2 How do multi-modal pretext tasks impact representations?

Multi-modal pretext tasks improve fine-tuning and linear probing. Using multi-pretext tasks improved both the FT and LP performance (see Table 4), except for the Cashew1k dataset. While MAE are known for good fine-tuning performance, the gap to the linear probing performance remains large [22, 52].

Table 3: Domain specific pretraining on optical images. Fine-tuning (FT) and linear probing (LP) performance using MAE pretrained on ImageNet (RGB), Sentinel-2 RGB (MMEarth-S2rgb), and Sentinel-2 multi-spectral (MMEarth-S2). Lowering the patch-size is crucial to adopt to the smaller medium resolution satellite images. Using all the 12 bands improves accuracy. Domain specific pretraining improves both FT and LP results. Higher is better for all metrics.

Pretrain data	Image Patch		BigEarth20k	So2Sat20k	Cashew1k	SACrop3k
	size	size	FT/LP	FT/LP	FT	FT
ImageNet	224	32	72.9/57.2	44.5/ 34.9	77.5	27.4
MMEarth-S2rgb	128	32	71.4/57.6	37.8/27.6	79.6	26.5
MMEarth-S2rgb	128	16	78.2/62.5	46.3 /31.0	80.3	29.6
MMEarth-S2rgb	112	16	77.8/62.2	44.7/34.1	81.0	29.1
MMEarth-S2	112	16	78.6 / 64.5	46.2/28.6	84.5	33.3

The representations learned from our multi-pretext objective substantially improved LP performance and provide a mechanism towards closing this performance gap. We observed an improvement of 3.7pp on BigEarth20k and 15.6pp on So2Sat20k with respect to pretraining on Sentinel-2 only. On So2Sat20k, the local climate zone classification, fine-tuning improves substantially (+9.7pp), indicating that the additional pretext tasks yield better representations that cannot be learned from MIM only. Here, we report results obtained with the task uncertainty loss. We found that both loss settings work equally well on these downstream tasks (see supplementary). The learned task uncertainties provide interesting insights, *e.g.* the uncertainty for the latitude (N-S) being lower than for the longitude (W-E), which could be explained by the rainfall and vegetation gradients along the North-South axis shaping the appearance of landscapes.

Pixel-level and image-level pretext tasks are useful. To study the role of the two groups of pretext tasks, we ran experiments where the Sentinel-2 reconstruction task was extended with only one group (Table 4). For the image-level downstream tasks, pretraining with only image-level pretext tasks achieved comparable performance to pretraining with all multi-modal pretext tasks. For So2Sat20k we observed that the image-level tasks had a strong effect, possibly because ERA5 climate variables serve as a good proxy task, but further experiments would be required to understand the importance of individual pretext tasks. While we expected that pixel-level pretext tasks might be more beneficial for segmentation tasks this was not confirmed.

Multi-modal pretext tasks improve label efficiency. Real-world applications often lack large amount of labelled data. To explore the benefits of pretraining in a limited label regime, we evaluated the LP performance using stratified subsets of the fine-tuning datasets. In our most extreme few-shot setting, there were only 100 training samples (*i.e.* 2 samples/category in BigEarth20k). Results in Fig. 3 show that models pretrained on all modalities in MMEarth outperformed models trained on only Sentinel-2 or only ImageNet in few-shot linear probing. While pretraining on MMEarth-S2 outperforms ImageNet pretraining in fine-tuning (Table 4), this does not always hold for linear probing. While,

Table 4: Multi-modal pretext tasks. Fine-tuning (FT) and linear probing (LP) performance for multi-pretext pretraining (MMEarth) and masked image pretraining (ImageNet, MMEarth-S2). We also present multi-pretext results with subsets of modalities using only pixel-level (MMEarth-PixelM) or only image-level (MMEarth-ImageM) modalities in addition to the Sentinel-2 optical image reconstruction. Multi-pretext pretraining improves both FT and LP results. Higher is better for all metrics.

Pretrain	BigEarth20k	So2Sat20k	Cashew1k	SAcrop3k
	FT/LP	FT/LP	FT	FT
ImageNet	72.9/57.2	44.5/34.9	77.5	27.4
MMEarth-S2	78.6/64.5	46.2/28.6	84.5	33.3
MMEarth-PixelM	79.3/66.4	49.5/37.0	80.4	34.1
MMEarth-ImageM	81.3 /68.1	54.6/42.9	81.0	34.0
MMEarth	80.0/ 68.2	55.9 / 44.2	81.4	34.5

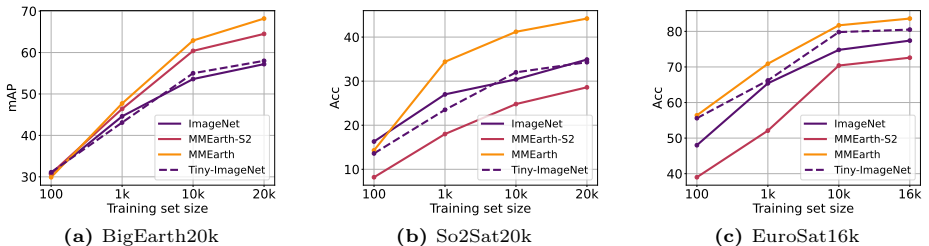


Fig. 3: Label efficiency for few-shot downstream performance. Linear probing performance for varying downstream dataset sizes. MP-MAE (‘Atto’) pretrained on ImageNet, MMEarth-S2 (multi-spectral only), MMEarth (all multi-modal pretext tasks). Tiny-ImageNet is the original ConvNext V2-MAE with a ‘Tiny’ backbone pretrained on ImageNet using the pretrained weights from [52].

EuroSat16k is an easy task where general image features learned on ImageNet are a strong baseline, we speculate that for So2Sat20k the texture in Sentinel-2 images alone is not a good pretraining signal.

Better parameter efficiency. Results from Fig. 3 show that our MP-MAE with an Atto encoder (3.7M parameters) pretrained with multi-modal pretext tasks outperformed a notably larger Tiny encoder (28M parameters) pretrained on ImageNet. Our encoder is not only smaller but was also only trained for 200 epochs compared to 800 epochs. This supports our motivation for creating better domain specific pretraining datasets and strategies instead of using larger models pretrained on generic image datasets like ImageNet.

Compares favourably to prior work. We compared our MP-MAE method to a small, but most closely related, subset of prior work in Table 5. While all models rely on different pretraining datasets and pretraining strategies, we show that our model compares favourably to prior work on most tasks, using fewer parameters in the encoder (3.7M for our MP-MAE versus 25M for ResNet-50).

Table 5: Comparison to prior work. We compare our multi-pretext pretraining with prior work that make use of different pretraining datasets and strategies. Our pretraining strategy achieve higher if not similar performance to other methods that use a ResNet-50 backbone. Higher is better for all metrics.

Method	Pretrain data (locations)	Encoder (parameters)	BigEarth20k	So2Sat20k	Cashew1k	SACrop3k
			FT/LP	FT/LP	FT	FT
GASSL [3]	fMoW (0.36M)	ResNet-50 (25M)	70.3/64.3	44.7/38.2	79.3	21.5
SeCO [29]	SeCo (0.20M)	ResNet-50 (25M)	77.6/ 71.8	47.6/40.8	78.9	24.4
SatlasPretrain [7]	SatlasPretrain (0.86M)	ResNet-50 (25M)	72.3/61.1	38.5/27.5	65.5	19.6
MP-MAE (ours)	MMEarth (1.24M)	ConvNeXt V2-Atto (3.7M)	80.0 /68.2	55.9 / 44.2	81.4	34.5

6.3 Limitations

While this study introduces a new dataset and methodology to advance the use of multiple modalities for representation learning, some limitations exist. First, we rely on GEO-Bench for downstream evaluation with five datasets covering a range of tasks and geographic regions. Further evaluation on diverse application domains from various geographical regions could reveal further insights in which scenarios our proposed multi-modal pretext tasks are beneficial. Second, we run our pretraining for 200 epochs due to restricted compute resources. For the same reason we only train encoders with limited number of parameters. Prior work exploring MAEs for representation learning pretrain for 800 or 1600 epochs. Pretraining for 200 epochs could be suboptimal for larger encoders. Third, our MP-MAE is not explicitly trained to be robust to varying number of input channels. We have trained the MP-MAE with multi-spectral Sentinel-2 images (12 bands). It needs to be investigated how our models transfer to downstream tasks that use RGB channels only. While this seems to be an artefact of benchmark datasets, rather than a real-world scenario when working with Sentinel-2 images, prior work proposed input masking strategies to make a model robust against missing channels [45], which could be built into our framework.

7 Conclusion

Prior work has mostly focused on exploiting *geolocation* and *time* for representation learning with EO data. We move a step forward and present MMEarth, a global *multi-modal* pretraining dataset for geospatial representation learning. With 12 modalities sampled from 1.2M locations, we propose a Multi-Pretext Masked Autoencoder (MP-MAE) approach based on ConvNeXt V2 to study the potential of aligned multi-modal data to learn better representations for Sentinel-2 optical satellite images. First, we show how to adapt the ConvNeXt V2 encoder to improve domain specific pretraining with medium-resolution satellite images. Second, we demonstrate that multi-modal pretext tasks are beneficial to learn better representations for Sentinel-2. Both fine-tuning and linear probing is improved, the latter profits substantially. This is promising for real-world applications with limited training data. However, further research is needed to close the gap between fine-tuning and linear-probing performance.

Acknowledgments. We greatly appreciate the open data policies of the Copernicus program and its partners ESA and ECMWF. We thank Google Earth Engine for hosting the data and providing free access. VN, CI, SB, and NL acknowledge support by the Pioneer Centre for AI, Danish National Research Foundation grant number P1. SO, AK, CI, and NL acknowledge support by the research grant DeReEco (grant number 34306) from Villum Foundation.

References

1. Argaw, D.M., Lee, J.Y., Woodson, M., Kweon, I.S., Caba Heilbron, F.: Long-range multimodal pretraining for movie understanding. In: International Conference on Computer Vision (ICCV). IEEE (2023). <https://doi.org/10.1109/iccv51070.2023.01232>, <http://dx.doi.org/10.1109/ICCV51070.2023.01232> 4
2. Assran, M., Duval, Q., Misra, I., Bojanowski, P., Vincent, P., Rabbat, M., LeCun, Y., Ballas, N.: Self-supervised learning from images with a joint-embedding predictive architecture. In: Computer Vision and Pattern Recognition (CVPR). pp. 15619–15629 (2023) 1
3. Ayush, K., Uzkent, B., Meng, C., Tanmay, K., Burke, M., Lobell, D., Ermon, S.: Geography-aware self-supervised learning. In: International Conference on Computer Vision (ICCV). pp. 10181–10190 (2021) 5, 14
4. Bachmann, R., Mizrahi, D., Atanov, A., Zamir, A.: Multimae: Multi-modal multi-task masked autoencoders. In: European Conference on Computer Vision (ECCV). pp. 348–367. Springer (2022) 2, 4, 9
5. Balestriero, R., Ibrahim, M., Sobal, V., Morcos, A., Shekhar, S., Goldstein, T., Bordes, F., Bardes, A., Mialon, G., Tian, Y., et al.: A cookbook of self-supervised learning. arXiv preprint arXiv:2304.12210 (2023) 1
6. Bardes, A., Garrido, Q., Ponce, J., Rabbat, M., LeCun, Y., Assran, M., Ballas, N.: Revisiting feature prediction for learning visual representations from video. arXiv preprint (2024) 3
7. Bastani, F., Wolters, P., Gupta, R., Ferdinando, J., Kembhavi, A.: Satlaspretrain: A large-scale dataset for remote sensing image understanding. In: International Conference on Computer Vision (ICCV). pp. 16772–16782 (2023) 4, 5, 14
8. Brown, C.F., Brumby, S.P., Guzder-Williams, B., Birch, T., Hyde, S.B., Mazzariello, J., Czerwinski, W., Pasquarella, V.J., Haertel, R., Ilyushchenko, S., et al.: Dynamic world, near real-time global 10 m land use land cover mapping. *Scientific Data* 9(1), 251 (2022) 4
9. Choy, C., Gwak, J., Savarese, S.: 4d spatio-temporal convnets: Minkowski convolutional neural networks. In: Computer Vision and Pattern Recognition (CVPR). pp. 3075–3084 (2019) 3, 8
10. Christie, G., Fendley, N., Wilson, J., Mukherjee, R.: Functional map of the world. In: Computer Vision and Pattern Recognition (CVPR). pp. 6172–6180 (2018) 4
11. Cong, Y., Khanna, S., Meng, C., Liu, P., Rozi, E., He, Y., Burke, M., Lobell, D., Ermon, S.: Satmae: Pre-training transformers for temporal and multi-spectral satellite imagery. *Advances in Neural Information Processing Systems (NeurIPS)* 35, 197–211 (2022) 5
12. Daudt, R.C., Wulf, H., Hafner, E.D., Bühler, Y., Schindler, K., Wegner, J.D.: Snow depth estimation at country-scale with high spatial and temporal resolution. *ISPRS Journal of Photogrammetry and Remote Sensing* 197, 105–121 (2023) 4

13. Deng, J., Dong, W., Socher, R., Li, L.J., Li, K., Fei-Fei, L.: Imagenet: A large-scale hierarchical image database. In: *Computer Vision and Pattern Recognition (CVPR)*. pp. 248–255. Ieee (2009) [2](#), [5](#)
14. Devlin, J., Chang, M.W., Lee, K., Toutanova, K.: BERT: Pre-training of deep bidirectional transformers for language understanding. In: Burstein, J., Doran, C., Solorio, T. (eds.) *Proceedings of the 2019 Conference of the North American Chapter of the Association for Computational Linguistics: Human Language Technologies, Volume 1 (Long and Short Papers)*. pp. 4171–4186. Association for Computational Linguistics, Minneapolis, Minnesota (2019). <https://doi.org/10.18653/v1/N19-1423>, <https://aclanthology.org/N19-1423> [3](#)
15. Dinerstein, E., Olson, D., Joshi, A., Vynne, C., Burgess, N.D., Wikramanayake, E., Hahn, N., Palminteri, S., Hedao, P., Noss, R., Hansen, M., Locke, H., Ellis, E.C., Jones, B., Barber, C.V., Hayes, R., Kormos, C., Martin, V., Crist, E., Sechrest, W., Price, L., Baillie, J.E.M., Weeden, D., Suckling, K., Davis, C., Sizer, N., Moore, R., Thau, D., Birch, T., Potapov, P., Turubanova, S., Tyukavina, A., de Souza, N., Pintea, L., Brito, J.C., Llewellyn, O.A., Miller, A.G., Patzelt, A., Ghazanfar, S.A., Timberlake, J., Klöser, H., Shennan-Farpón, Y., Kindt, R., Lillesø, J.P.B., van Breugel, P., Graudal, L., Voge, M., Al-Shammari, K.F., Saleem, M.: An ecoregion-based approach to protecting half the terrestrial realm. *BioScience* **67**(6), 534–545 (2017). <https://doi.org/10.1093/biosci/bix014>, <http://dx.doi.org/10.1093/biosci/bix014> [4](#), [6](#), [7](#), [21](#)
16. Dosovitskiy, A., Beyer, L., Kolesnikov, A., Weissenborn, D., Zhai, X., Unterthiner, T., Dehghani, M., Minderer, M., Heigold, G., Gelly, S., Uszkoreit, J., Houlsby, N.: An image is worth 16x16 words: Transformers for image recognition at scale. In: *International Conference on Learning Representations (ICLR)* (2021), <https://openreview.net/forum?id=YicbFdNTTy> [3](#)
17. Dubayah, R., Blair, J.B., Goetz, S., Fatoyinbo, L., Hansen, M., Healey, S., Hofton, M., Hurtt, G., Kellner, J., Luthcke, S., et al.: The global ecosystem dynamics investigation: High-resolution laser ranging of the earth’s forests and topography. *Science of remote sensing* **1**, 100002 (2020) [7](#)
18. Feichtenhofer, C., Fan, H., Li, Y., He, K.: Masked autoencoders as spatiotemporal learners. In: Oh, A.H., Agarwal, A., Belgrave, D., Cho, K. (eds.) *Advances in Neural Information Processing Systems (NeurIPS)* (2022), <https://openreview.net/forum?id=UaXD4A13mdb> [3](#)
19. Geng, X., Liu, H., Lee, L., Schuurmans, D., Levine, S., Abbeel, P.: Multimodal masked autoencoders learn transferable representations (2022) [4](#)
20. Ghiasi, G., Zoph, B., Cubuk, E.D., Le, Q.V., Lin, T.Y.: Multi-task self-training for learning general representations. In: *International Conference on Computer Vision (ICCV)*. pp. 8856–8865 (2021) [4](#)
21. Gorelick, N., Hancher, M., Dixon, M., Ilyushchenko, S., Thau, D., Moore, R.: Google earth engine: Planetary-scale geospatial analysis for everyone. *Remote Sensing of Environment* **202**, 18–27 (2017) [2](#), [6](#), [20](#)
22. He, K., Chen, X., Xie, S., Li, Y., Dollár, P., Girshick, R.: Masked autoencoders are scalable vision learners. In: *Computer Vision and Pattern Recognition (CVPR)*. pp. 16000–16009 (2022) [1](#), [3](#), [4](#), [10](#), [11](#)
23. Helber, P., Bischke, B., Dengel, A., Borth, D.: Eurosat: A novel dataset and deep learning benchmark for land use and land cover classification. *IEEE Journal of Selected Topics in Applied Earth Observations and Remote Sensing* **12**(7), 2217–2226 (2019) [10](#)

24. Kendall, A., Gal, Y., Cipolla, R.: Multi-task learning using uncertainty to weigh losses for scene geometry and semantics. In: Computer Vision and Pattern Recognition (CVPR). pp. 7482–7491 (2018) [9](#)
25. Klemmer, K., Rolf, E., Robinson, C., Mackey, L., Rufwurm, M.: Satclip: Global, general-purpose location embeddings with satellite imagery. arXiv preprint arXiv:2311.17179 (2023) [5](#)
26. Kruitwagen, L., Story, K., Friedrich, J., Byers, L., Skillman, S., Hepburn, C.: A global inventory of photovoltaic solar energy generating units. *Nature* **598**(7882), 604–610 (2021) [4](#)
27. Lacoste, A., Lehmann, N., Rodriguez, P., Sherwin, E.D., Kerner, H., Lütjens, B., Irvin, J.A., Dao, D., Alemohammad, H., Drouin, A., Gunturkun, M., Huang, G., Vazquez, D., Newman, D., Bengio, Y., Ermon, S., Zhu, X.X.: GEO-bench: Toward foundation models for earth monitoring. In: Thirty-seventh Conference on Neural Information Processing Systems Datasets and Benchmarks Track (2023), <https://openreview.net/forum?id=IptxZvA3at> [2](#), [6](#), [9](#), [10](#)
28. Lang, N., Jetz, W., Schindler, K., Wegner, J.D.: A high-resolution canopy height model of the earth. *Nature Ecology & Evolution* **7**(11), 1778–1789 (2023) [4](#), [7](#)
29. Manas, O., Lacoste, A., Giró-i Nieto, X., Vazquez, D., Rodriguez, P.: Seasonal contrast: Unsupervised pre-training from uncurated remote sensing data. In: International Conference on Computer Vision (ICCV). pp. 9414–9423 (2021) [5](#), [14](#)
30. Microsoft Open Source, McFarland, M., Emanuele, R., Morris, D., Augspurger, T.: microsoft/planetarycomputer: October 2022 (Oct 2022), <https://doi.org/10.5281/zenodo.7261897> [2](#)
31. Mizrahi, D., Bachmann, R., Kar, O.F., Yeo, T., Gao, M., Dehghan, A., Zamir, A.: 4m: Massively multimodal masked modeling. In: Thirty-seventh Conference on Neural Information Processing Systems (2023), <https://openreview.net/forum?id=TegmlsD8oQ> [2](#), [4](#)
32. Mohamed, A., Lee, H., Borgholt, L., Havtorn, J.D., Edin, J., Igel, C., Kirchhoff, K., Li, S.W., Livescu, K., Maaløe, L., Sainath, T.N., Watanabe, S.: Self-supervised speech representation learning: A review. *IEEE Journal of Selected Topics in Signal Processing* **16**(6), 1179–1210 (2022) [1](#)
33. Oquab, M., Darcet, T., Moutakanni, T., Vo, H.V., Szafraniec, M., Khalidov, V., Fernandez, P., Haziza, D., Massa, F., El-Nouby, A., Howes, R., Huang, P.Y., Xu, H., Sharma, V., Li, S.W., Galuba, W., Rabbat, M., Assran, M., Ballas, N., Synnaeve, G., Misra, I., Jegou, H., Mairal, J., Labatut, P., Joulin, A., Bojanowski, P.: Dinov2: Learning robust visual features without supervision (2023) [1](#)
34. Pathak, D., Krahenbuhl, P., Donahue, J., Darrell, T., Efros, A.A.: Context encoders: Feature learning by inpainting. In: Computer Vision and Pattern Recognition (CVPR). pp. 2536–2544 (2016) [3](#)
35. Planet, Radiant Earth Foundation, Western Cape Department of Agriculture, German Aerospace Center (DLR): A fusion dataset for crop type classification in Western Cape, South Africa (2021). <https://doi.org/10.34911/RDNT.GQY868>, <https://registry.mlhub.earth/10.34911/rdnt.gqy868> [10](#)
36. Radford, A., Kim, J.W., Hallacy, C., Ramesh, A., Goh, G., Agarwal, S., Sastry, G., Askell, A., Mishkin, P., Clark, J., et al.: Learning transferable visual models from natural language supervision. In: International Conference on Machine Learning (ICML). pp. 8748–8763. PMLR (2021) [2](#), [4](#)
37. Reed, C.J., Gupta, R., Li, S., Brockman, S., Funk, C., Clipp, B., Keutzer, K., Candido, S., Uyttendaele, M., Darrell, T.: Scale-mae: A scale-aware masked autoencoder for multiscale geospatial representation learning. In: International Conference on Computer Vision (ICCV). pp. 4088–4099 (2023) [2](#), [5](#)

38. Ronneberger, O., Fischer, P., Brox, T.: U-net: Convolutional networks for biomedical image segmentation. In: Medical Image Computing and Computer-Assisted Intervention (MICCAI). pp. 234–241. Springer (2015) **8**, **11**
39. Rufwurm, M., Venkatesa, S.J., Tuia, D.: Large-scale detection of marine debris in coastal areas with sentinel-2. *Iscience* **26**(12) (2023) **4**
40. de Sa, V.R., Ballard, D.H.: Category learning through multimodality sensing. *Neural Computation* **10**(5), 1097–1117 (1998). <https://doi.org/10.1162/089976698300017368>, <http://dx.doi.org/10.1162/089976698300017368> **3**
41. Sumbul, G., Charfuelan, M., Demir, B., Markl, V.: Bigearthnet: A large-scale benchmark archive for remote sensing image understanding. In: IGARSS 2019-2019 IEEE International Geoscience and Remote Sensing Symposium. pp. 5901–5904. IEEE (2019) **4**, **10**
42. Sumbul, G., De Wall, A., Kreuziger, T., Marcelino, F., Costa, H., Benevides, P., Caetano, M., Demir, B., Markl, V.: Bigearthnet-mm: A large-scale, multimodal, multilabel benchmark archive for remote sensing image classification and retrieval [software and data sets]. *IEEE Geoscience and Remote Sensing Magazine* **9**(3), 174–180 (2021) **4**
43. Tolan, J., Yang, H.I., Nosarzewski, B., Couairon, G., Vo, H.V., Brandt, J., Spore, J., Majumdar, S., Haziza, D., Vamaraju, J., Moutakanni, T., Bojanowski, P., Johns, T., White, B., Tiedeke, T., Couprie, C.: Very high resolution canopy height maps from RGB imagery using self-supervised vision transformer and convolutional decoder trained on aerial lidar. *Remote Sensing of Environment* **300**, 113888 (2024). <https://doi.org/10.1016/j.rse.2023.113888>, <https://www.sciencedirect.com/science/article/pii/S003442572300439X> **4**
44. Tong, Z., Song, Y., Wang, J., Wang, L.: VideoMAE: Masked autoencoders are data-efficient learners for self-supervised video pre-training. In: Oh, A.H., Agarwal, A., Belgrave, D., Cho, K. (eds.) *Advances in Neural Information Processing Systems (NeurIPS)* (2022), <https://openreview.net/forum?id=AhccnBXSne> **3**
45. Tseng, G., Zvonkov, I., Purohit, M., Rolnick, D., Kerner, H.: Lightweight, pre-trained transformers for remote sensing timeseries. *arXiv preprint arXiv:2304.14065* (2023) **5**, **14**
46. Tucker, C., Brandt, M., Hiernaux, P., Kariryaa, A., Rasmussen, K., Small, J., Igel, C., Reiner, F., Melocik, K., Meyer, J., et al.: Sub-continental-scale carbon stocks of individual trees in african drylands. *Nature* **615**(7950), 80–86 (2023) **4**
47. Van Horn, G., Cole, E., Beery, S., Wilber, K., Belongie, S., Mac Aodha, O.: Benchmarking representation learning for natural world image collections. In: *Computer Vision and Pattern Recognition (CVPR)*. pp. 12884–12893 (2021) **2**
48. Vandenhende, S., Georgoulis, S., Van Gansbeke, W., Proesmans, M., Dai, D., Van Gool, L.: Multi-task learning for dense prediction tasks: A survey. *IEEE Transactions on Pattern Analysis and Machine Intelligence* **44**(7), 3614–3633 (2021) **9**
49. Vincent, P., Larochelle, H., Bengio, Y., Manzagol, P.A.: Extracting and composing robust features with denoising autoencoders. In: *International Conference on Machine Learning (ICML)*. p. 1096–1103. ACM (2008). <https://doi.org/10.1145/1390156.1390294>, <https://doi.org/10.1145/1390156.1390294> **3**
50. Wang, Y., Braham, N.A.A., Xiong, Z., Liu, C., Albrecht, C.M., Zhu, X.X.: SSL4EO-S12: A large-scale multi-modal, multi-temporal dataset for self-supervised learning in earth observation. *arXiv preprint arXiv:2211.07044* (2022) **4**
51. Wei, C., Fan, H., Xie, S., Wu, C.Y., Yuille, A., Feichtenhofer, C.: Masked feature prediction for self-supervised visual pre-training. In: *Computer Vision and Pattern Recognition (CVPR)*. pp. 14668–14678 (2022) **3**, **4**

52. Woo, S., Debnath, S., Hu, R., Chen, X., Liu, Z., Kweon, I.S., Xie, S.: ConvNeXt V2: Co-designing and scaling convnets with masked autoencoders. In: Computer Vision and Pattern Recognition (CVPR). pp. 16133–16142 (2023) [2](#), [3](#), [8](#), [9](#), [11](#), [13](#)
53. Xie, Z., Zhang, Z., Cao, Y., Lin, Y., Bao, J., Yao, Z., Dai, Q., Hu, H.: SimMIM: A simple framework for masked image modeling. In: Computer Vision and Pattern Recognition (CVPR). pp. 9653–9663 (2022) [3](#), [11](#)
54. Yin, L., Ghosh, R., Lin, C., Hale, D., Weigl, C., Obarowski, J., Zhou, J., Till, J., Jia, X., You, N., Mao, T., Kumar, V., Jin, Z.: Mapping smallholder cashew plantations to inform sustainable tree crop expansion in benin. *Remote Sensing of Environment* **295**, 113695 (Sep 2023), <http://dx.doi.org/10.1016/j.rse.2023.113695> [10](#)
55. Yu, X., Tang, L., Rao, Y., Huang, T., Zhou, J., Lu, J.: Point-BERT: Pre-training 3D point cloud transformers with masked point modeling. In: Computer Vision and Pattern Recognition (CVPR). pp. 19313–19322 (2022) [3](#)
56. Zamir, A.R., Sax, A., Shen, W., Guibas, L.J., Malik, J., Savarese, S.: Taskonomy: Disentangling task transfer learning. In: Computer Vision and Pattern Recognition (CVPR). pp. 3712–3722 (2018) [4](#)
57. Zhu, X.X., Hu, J., Qiu, C., Shi, Y., Kang, J., Mou, L., Bagheri, H., Haberle, M., Hua, Y., Huang, R., Hughes, L., Li, H., Sun, Y., Zhang, G., Han, S., Schmitt, M., Wang, Y.: So2sat lcz42: A benchmark data set for the classification of global local climate zones [software and data sets]. *IEEE Geoscience and Remote Sensing Magazine* **8**(3), 76–89 (2020). <https://doi.org/10.1109/MGRS.2020.2964708> [10](#)

A Dataset details for MMEarth

MMEarth was collected at 1.2M locations around the world. The data was first downloaded at tile size of $1300\text{m} \times 1300\text{m}$ corresponding to approximately 130×130 pixels. As this can lead to slight variations by ± 1 pixel, we center cropped to 128×128 pixels to harmonize the final tile size. The total dataset is 639GB in size and offered as a compressed gzip hdf5 file (lossless compression).

Fig. A1 and Fig. A2 show the spatial and temporal distribution of Sentinel-2 L1C (top of atmosphere) and L2A (bottom of atmosphere) data. The atmospherically corrected L2A data is globally available on Google Earth Engine [21] (GEE) starting November 2018 until today. Before November 2018, L2A only exists in certain parts of the world (*e.g.* Europe). Hence, to get a uniform distribution of samples throughout the four years 2017-2020, we ensured that L1C is sampled more frequently between January 2017 and November 2018. From December 2018, we have randomly sampled L1C or L2A data to guarantee that later years are also covered by both product levels.

The distribution of additional modalities is visualized in Fig. A3. Due to our biome-balanced sampling scheme, described in the following section, the MMEarth dataset focuses on the natural world, but also contains some built-up landcover. Thus, MMEarth was designed as a pretraining dataset for applications in environmental monitoring.

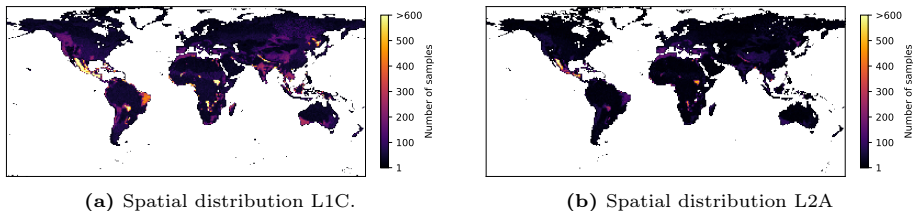


Fig. A1: Spatial distribution of L1C and L2A data.

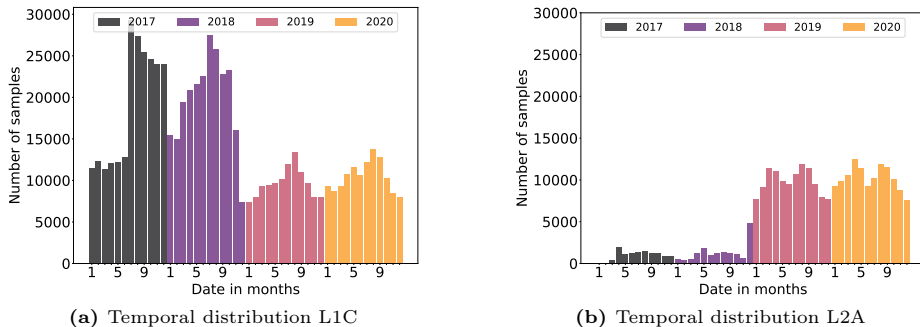


Fig. A2: Temporal distribution of l1c and l2a data.

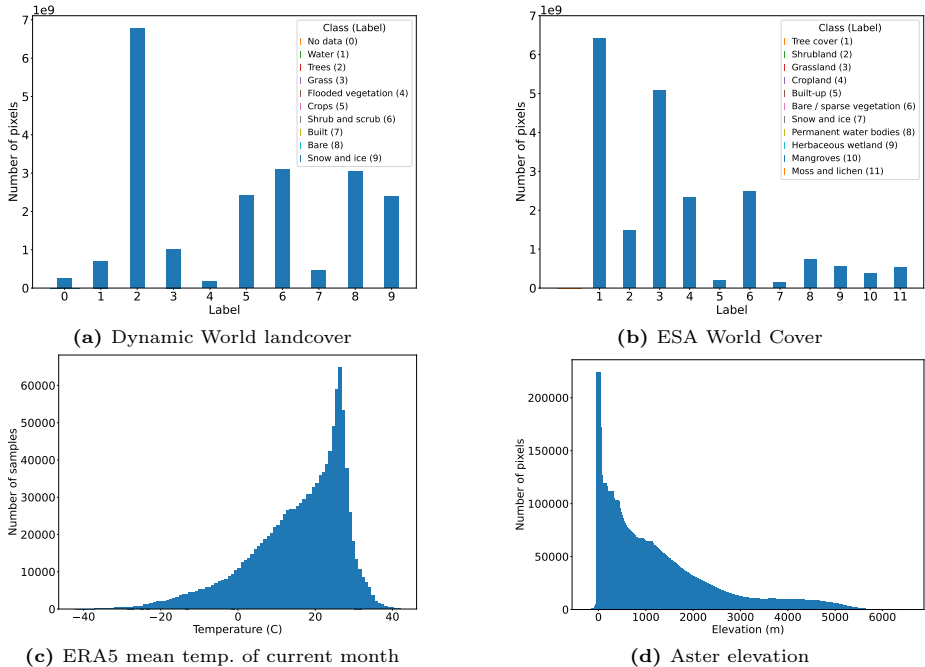


Fig. A3: Distribution of additional modalities.

A.1 Sampling strategy

Sampling of locations. MMEarth was collected, ensuring uniform sampling across 14 biomes [15]. Each biome can further be divided into a number of ecoregions. We used the GEE toolbox for this stratified sampling approach. However, since the area of the largest biome was too large to be processed by GEE, we facilitate stratified sampling by considering the area within an ecoregion. The number of samples per ecoregion was computed by

$$N_e = \frac{N_t}{14} \cdot \frac{A_e}{A_{B_e}}, \quad (2)$$

where N_e is the number of samples for an ecoregion, N_t is the total number of samples to collect (1.2M in our case), A_e is the area covered by that ecoregion, A_{B_e} is the area covered by the biome the ecoregion is part of and 14 represents the number of biomes. This process was repeated for all ecoregions and for all biomes to finally obtain a uniform sample across the biomes.

Sampling of Sentinel-2. For every location, we first randomly chose a year from 2017-2020. For the selected year, we randomly sampled either L1C and L2A. If no L2A data existed, we sampled L1C data (since L2A is not globally

available until November 2018). We queried the respective Sentinel-2 data collection with *CLOUD_PIXEL_PERCENTAGE* of less than 10% at the original 100km×100km tile level. We discarded images that contain no data values at the boundary of the orbit coverage. From this collection of candidates, we randomly sampled one Sentinel-2 image date. Finally we cropped the respective tile centered at the query location. We downloaded all bands (*i.e.* 13 for L1C and 12 for L2A) and reprojected all bands to a 10m resolution using bilinear interpolation. For our experiments, we always used the 12 bands corresponding to the L2A product, excluding band B10 in L1C.

We found that the cloud filter at the original tile level mostly led to cloud free samples, but some samples contained clouds. In our experiments, we did not apply any cloud filtering at the sample level, although that would be possible with the information provided in MMEarth.

Sampling and processing of additional modalities. In this sub-section, we explain any additional processing done when sampling modalities. We only focus on those modalities that require additional processing apart from the ones performed when requesting for data using the GEE API. All pixel-level modalities were reprojected to 10m Sentinel-2 grid using bilinear interpolation.

Sentinel-1. Sentinel-1 data was sampled with reference to the sampled Sentinel-2 observation date. Hence, we sampled the closest Sentinel-1 image from both the ascending and descending orbits. We downloaded all four available bands.

Aster GDEM. Aster data from GEE includes an elevation band, from which we have computed the slope.

Dynamic World. We first sampled the dynamic world collection for the full year of the Sentinel-2 observation date. The data from GEE comes with labels from 0 to 8. We also realized that *NO_DATA* values are also mapped to 0. Hence, we mapped the labels from 0 to 9, and indicated 0 to be the *NO_DATA* pixels. We then compute the mode of the full collection. This was done since dynamic world images for a specific date can sometimes lead to *NO_DATA* values, and hence to reduce the amount of such pixels, we computed the mode of a set of images.

ERA5. We selected 4 bands from the ERA5 dataset on GEE (average temperature, minimum temperature, maximum temperature and total precipitation). These statistics are monthly. Additionally, we computed the yearly average, minimum, maximum, and total, respectively, for each of these statistics. We collected 3 sets of statistics for the same month, previous month, and full year corresponding to the Sentinel-2 observation date (*3 sets × 4 bands = 12 bands*).

Geolocation. We use a cyclic encoding of the latitude and longitude corresponding to the center point as follows:

$$Lat_{sin} = \sin(2\pi Lat/360) \tag{3}$$

$$Lat_{cos} = \cos(2\pi Lat/360) \tag{4}$$

$$Lon_{sin} = \sin(2\pi Lon/360) \quad (5)$$

$$Lon_{cos} = \cos(2\pi Lon/360) \quad (6)$$

Date. Similarly, we use a cyclic encoding of the month of the Sentinel-2 observation date:

$$Month_{sin} = \sin(2\pi m/12) \quad (7)$$

$$Month_{cos} = \cos(2\pi m/12) \quad (8)$$

where m , corresponds to the month as an integer from 1 to 12.

A.2 Licenses of data sources

MMEarth is constructed from publicly available data distributed under non-restrictive licenses. We list the license for every data source in Table A1. The MMEarth dataset is released under the CC BY 4.0 license.

Table A1: Licenses of data sources. All collected data is licensed for open usage. The detailed license information is listed for each data source. All urls were accessed 2024-03-11.

Data source	License	Info
Sentinel-2	CC BY-SA 3.0 IGO	https://open.esa.int/copernicus-sentinel-satellite-imagery-under-open-licence/
Sentinel-1	CC BY-SA 3.0 IGO	https://open.esa.int/copernicus-sentinel-satellite-imagery-under-open-licence/
Aster GDEM v3	similar to CC0	https://lpdaac.usgs.gov/data/data-citation-and-policies/
ETH-GCHM	Creative Commons Attribution 4.0 International	https://langnico.github.io/globalcanopyheight
Dynamic World	Creative Commons BY-4.0	https://dynamicworld.app/about/
ESA World Cover	Creative Commons Attribution 4.0 International	https://esa-worldcover.org/en/data-access#citation
Bioime	Creative Commons Attribution 4.0 International	https://ecoregions.appspot.com/
Ecoregion	Creative Commons Attribution 4.0 International	https://ecoregions.appspot.com/
ERA5	Copernicus C3S/CAMS License agreement	https://www.ecmwf.int/en/forecasts/dataset/ecmf-reanalysis-v5

B Implementation details for evaluation

So2Sat20k only provides 10 instead of 12 bands. However, to make use of these additional multi-spectral bands, we filled in the missing bands (B1 and B9) with a copy of the band with the closest wavelength. I.e., we use a copy of B2 for B1, and B8A for B9. This could lead to a lower linear probing performance but should not affect results much when fine-tuning the entire encoder. To adapt to these slight distribution shifts in band B1 and B9, we ran an extended linear probing, where the parameters of the first convolution layer are updated in addition to the last linear layer. Results from Table A2 show that this extended linear probing improved performance compared to linear probing on So2Sat20k.

Table A2: Extended linear probing on So2Sat20k. Extended linear probing experiments with updating the parameters of the first convolution layer in addition to the last layer.

(a) Pretraining on MMEarth-S2		(b) Pretraining on MMEarth	
So2Sat20k		So2Sat20k	
LP	28.6	LP	44.2
LP + first layer	37.0	LP + first layer	49.8

C Taster pretraining datasets: MMEarth100k and MMEarth64

To facilitate research in self-supervised learning with limited compute resources, we provide two subsets of the MMEarth dataset: MMEarth100k and MMEarth64. The MMEarth100k is a random subset of 100k locations with the full 128×128 pixels and has a data volume of roughly 48GB. The MMEarth64 contains all 1.2M locations, but all modalities are center cropped to obtain rasters of 64×64 pixels, which reduces the data volume roughly by factor 4 from 639GB to 163GB.

We provide results using these taster subsets to pretrain our MP-MAE approach with the same setting as used for pretraining on the full MMEarth dataset in Table A3. The only change required for MMEarth64 is the patch size. As the image size is halved from 112 to 56 pixels, we also half the patch size from 16 to 8 pixels which keeps the number of patches the same. We observe that pretraining on MMEarth64 performs comparably to MMEarth, and even slightly better in some tasks. Pretraining on MMEarth100k lead to a substantial drop in performance, but still outperforms the ImageNet pretrained models on BigEarth20k and SAcrop3k. From these initial results, we conclude that the diversity and number of samples is more important than the size of the receptive field for learning generalizing representations.

Table A3: MP-MAE results on taster datasets.

Pretrain data	Image Patch		BigEarth20k	So2Sat20k	Cashew1k	SAcrop3k
	size	size	FT/LP	FT/LP	FT	FT
ImageNet	224	32	72.9/57.2	44.5/34.9	77.5	27.4
MMEarth	112	16	80.0/68.2	55.9/44.2	81.4	34.5
MMEarth100k	112	16	75.5/63.3	42.9/31.4	68.4	30.6
MMEarth64	56	8	82.8/67.4	56.9/42.3	81.6	35.8

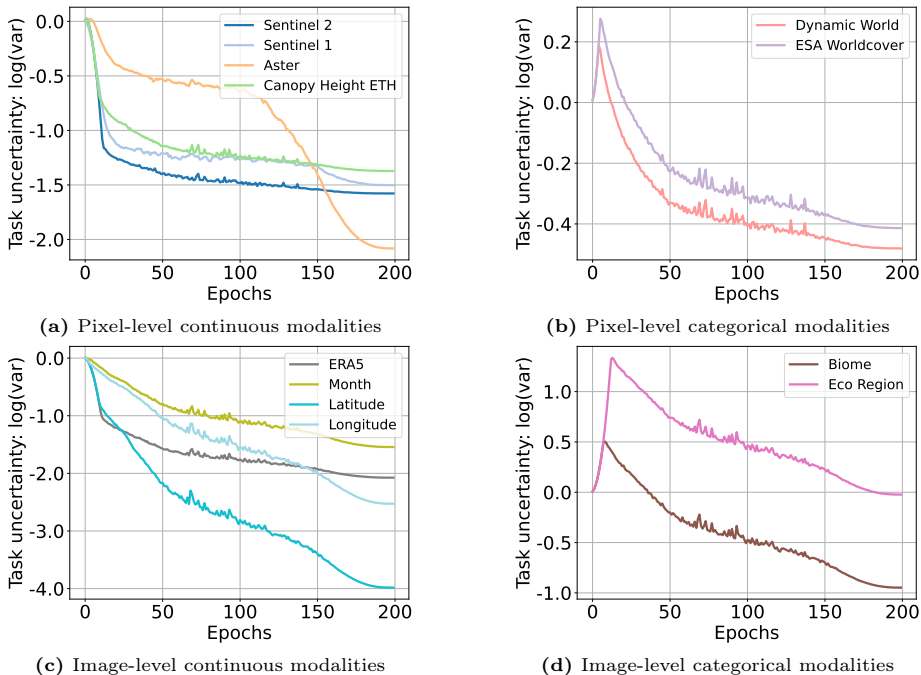


Fig. A4: Task uncertainty during pretraining. We plot the $\log(\text{var})$ for each task grouped by pixel-level *vs.* image-level and continuous *vs.* categorical tasks.

D Additional results

D.1 Ablation of multi-pretext loss strategy

Results from Table A5 show that for the Atto model, pretraining with uncertainty based loss weighting achieves comparable performance to equal weighting. While the performance is comparable, we note that uncertainty loss weighting provides additional insights on the importance of tasks during pretraining (see Fig. A4).

Analysis of the estimated task uncertainty We visualize the estimated task uncertainty over the pretraining grouped for comparable targets: pixel-continuous, image-continuous, pixel-categorical and image-categorical (see Fig. A4). For all tasks, the log variance decreases during pretraining. However, for the categorical tasks we observe an initial increase in uncertainty before a decrease. Interestingly, the relative weighting of tasks changes over epochs, *e.g.* within the pixel-continuous tasks, the Aster tasks (elevation, slope) have the highest uncertainty until epoch 150, before it drops to the lowest. A similar change in relative weight is observed for the ERA5 and Longitude. The latitude has a substantially lower uncertainty than the longitude, which can be explained by

the rainfall and vegetation gradients along the North-South axis that shape the features and appearance of landscapes.

D.2 Input normalization for downstream tasks

During pretraining, we compute the normalization statistics across the whole dataset for each modality (global statistics). In the case of Sentinel-2, we additionally compute separate statistics for L1C and L2A data. When evaluating on downstream tasks, we apply the normalization statistics computed over the downstream dataset. This can introduce a distribution shift when performing FT/LP. To avoid this, we run an experiment by applying the same global stats to the downstream evaluation tasks. Specifically, if the downstream task has been collected with Sentinel-2 L2A data (*e.g.* BigEarth20k), we apply the global statistics for L2A on this task. Results from Table A4 indicate that in the case of BigEarth20k, using global pretraining statistics can help improve the performance, but the improvement is not consistent for the other downstream tasks.

Table A4: Impact of input normalization for downstream learning. Results for the Atto model. Domain specific pretraining allows to transfer the input statistics of the pretraining to the downstream tasks. For downstream tasks using L2A (or L1C) data, we apply the corresponding pretraining L2A (or L1C) statistics. This reduces domain shifts between the pretraining and downstream tasks and facilitates FT and LP. We omit SACrop3k from these experiments because the benchmark dataset contains preprocessed data that are neither L1A nor L1C reflectance values.

Pretrain	FT/LP input normalization	BigEarth20k	So2Sat20k	Cashew1k
		FT/LP	FT/LP	FT
MMEarth FT/LP train stats		80.0/68.2	55.9/44.2	81.4
MMEarth Pretraining stats L2A		82.3/71.3	-	79.3
MMEarth Pretraining stats L1C		-	55.6/43.4	-

Table A5: Loss aggregation strategy. We evaluate the effect of the two loss aggregation strategies: Equal weighting *vs.* task uncertainty weighting.

Pretrain	Model	BigEarth20k	So2Sat20k	Cashew1k	SACrop3k
		FT/LP	FT/LP	FT	FT
MP-MAE (ours)	Atto-Uncertainty	80.0/68.2	55.9/44.2	81.4	34.5
MP-MAE (ours)	Atto-Equal	80.9/69.3	58.8/41.5	80.1	34.2

D.3 Qualitative reconstruction results

We visualize some reconstruction examples of the pixel-level pretraining tasks in Fig. A5. Similar to the results in the original ConvNeXt V2 paper, we observe that the reconstruction of the masked patches is rather blurry, but coarser patterns are captured. The visualization of the Sentinel-2 reconstruction is also affected by the patch-level normalization of the target. The reconstruction result of the visible patches is random, as the reconstruction loss was only optimized for non-visible patches. However, the goal of our MP-MAE approach is not to solve the pretext tasks, but to learn good semantic representations through these tasks. These results show that if we were to specialize on any of the pretraining task, then one option could be to fine-tune the pretrained model separately for each task.

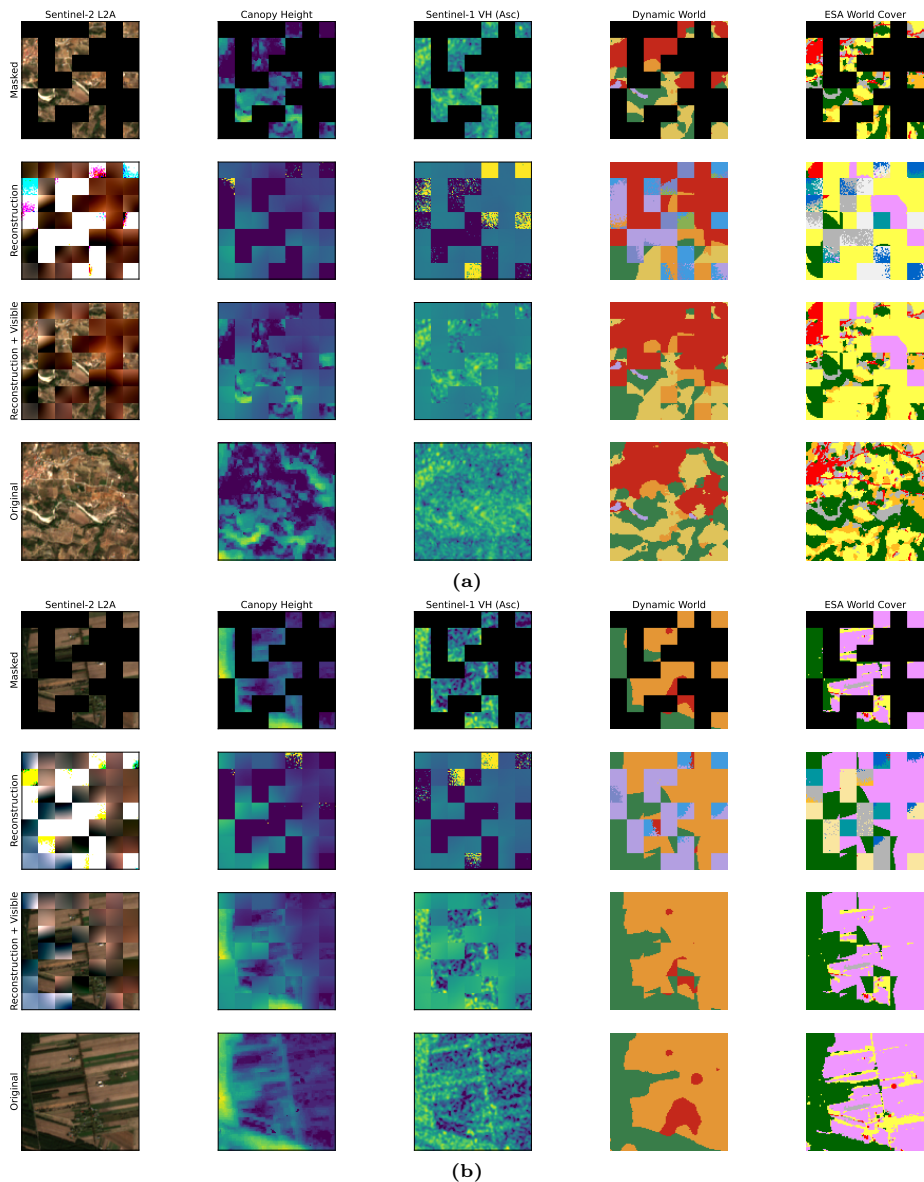


Fig. A5: Reconstruction results. Visualization of reconstruction examples for pixel-level pretraining tasks.